DOI: 10.61782/fa.2025.0670

FORUM ACUSTICUM EURONOISE 2025

PARAMETRIC STUDY OF TURBULENCE INGESTION NOISE FOR MARINE PROPELLERS

Romain Lavanant[1,2*] **Benjamin Cotté**[2] **Gilles Serre**[1]
Jean-François Mercier[3]
[1] Naval Group, CEMIS, Ollioules, France
[2] IMSIA, ENSTA, CNRS, CEA, EDF, Institut Polytechnique de Paris, France
[3] POEMS, CNRS, INRIA, ENSTA, Institut Polytechnique de Paris, France

ABSTRACT

Hydrodynamic noise is an important component of the overall noise radiated by a ship, particularly at low frequencies where propeller noise could be dominant especially at high speed. This study proposes a simplified analytical solution of the phenomenon of spectral humps of propeller noise due to the interaction between a rotating propeller and an incident turbulent flow. The acoustic radiation is described by the Ffowcs-Williams and Hawkings analogy in the compact approximation. The inflow turbulence field is assumed to be homogeneous and isotropic and is modeled using a von Kármán spectrum. Experimental validation and comparison with more costly analytical solutions demonstrate the ability of the developed model to correctly capture the characteristics of the humps related to turbulence ingestion. From the results obtained, a parametric analysis enables us to define a criterion for the emergence and shape of turbulence ingestion humps according to the propeller advance ratio, improving the criterion proposed by Ffowcs-Williams and Hawkings in 1969.

Keywords: *turbulence ingestion, marine propellers, noise prediction, spectral humps, parametric analysis*

**Corresponding author*: *romain.lavanant@ensta.fr.*

1. INTRODUCTION

In the context of propeller hydroacoustics, turbulence ingestion noise is due to the interaction between the rotating blades and the turbulent wake of a submarine or a surface vessel. The development of predictive models to better understand the physical origins of turbulence ingestion noise and estimating its levels is critical to enhance ship discretion. Understanding fundamental noise generation mechanisms allows architects to propose solutions like optimized blade and hull geometries or operational adjustments. Integrated early in design, it can reduce detectability by passive sonar in defense contexts and mitigate environmental impacts on marine life (Fig. 1).

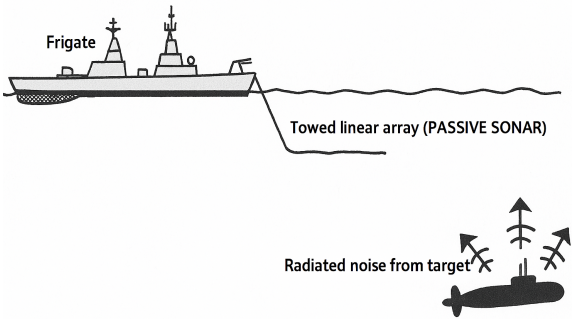

Figure 1. Detection of a submarine by passive SONAR in anti-submarine warfare.

This study targets low-frequency noise, specifically turbulence ingestion humps. When a turbulent flow is ingested by a rotating propeller, the incoming eddies are periodically chopped by the propeller. This interaction can potentially lead to a correlation (depending on the config-

uration) between the broadband turbulence spectrum and the periodic passage of the blades. This correlation creates a series of humps centered at blade passage frequency (BPF) harmonics on the resulting spectrum. The objective is to study the influence of propeller's parameters on the spectral humps and to define a criterion for the appearance of these humps, building on prior research to fully resolve turbulence-blade interactions while keeping computational costs industrially feasible.

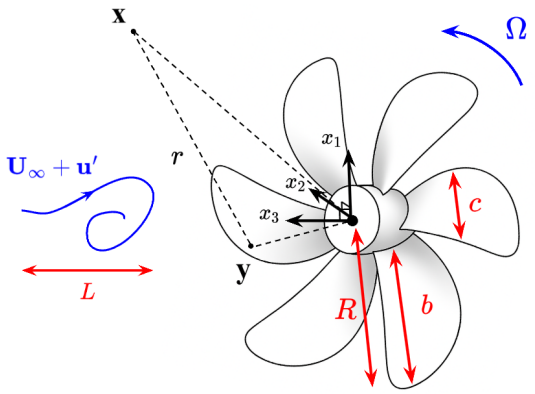

Figure 2. Fixed reference frame, with origin at the center of the propeller. $\boldsymbol{x}$ corresponds to the receiver's coordinate, and $\boldsymbol{y}$ to the coordinate within the volume containing the sources near the propeller (Ffowcs-Williams and Hawkings analogy).

2. NOISE RADIATION MODELING

To predict turbulence ingestion noise, this study employs a simplified version of the Ffowcs-Williams formulation for moving surfaces under the compact source approximation : $K_0 c < 1$, $K_0 R < 1$, where $K_0 = \omega/c_\infty$ is the acoustic wavenumber, c is the blade chord and R the propeller radius (see Fig. 2). For a propeller with N blades rotating at angular velocity Ω, the far-field ($|\boldsymbol{x}| \gg R$) acoustic pressure spectrum is thus expressed as in [1] section 6.6.2:

$$\widehat{p}(\boldsymbol{x},\omega) \simeq \frac{iK_j}{8\pi^2|\boldsymbol{x}|} e^{i\boldsymbol{K}\cdot\boldsymbol{x}} \widehat{F_j}(\omega), \tag{1}$$

with the acoustic wave vector in a convected medium:

$$\boldsymbol{K} = \frac{\omega}{c_\infty}\left(\frac{\boldsymbol{x}}{|\boldsymbol{x}|} - \boldsymbol{M}_\infty\right), \quad \boldsymbol{M}_\infty = (0,0,M_\infty), \tag{2}$$

$\widehat{F_j}(\omega)$ represents the force fluctuation spectrum and is expressed as [2],

$$\widehat{F_j}(\omega) = \sum_{n=0}^{N-1} \int_{-\infty}^{+\infty} \int_{S(\tau)} f_j(\boldsymbol{y}^{(n)},\tau) dS(\boldsymbol{y}^{(n)}) e^{i\omega\tau} d\tau, \tag{3}$$

with f_j is the surface force fluctuation, N the number of blades and S the surface of each blade. The radiated pressure spectral density in the far-field, is then derived as:

$$S_{pp}(\boldsymbol{x},\omega) \simeq \frac{K_i K_j}{64\pi^4|\boldsymbol{x}|^2} S_{F_iF_j}(\omega), \tag{4}$$

where the force spectral density $S_{F_iF_j}(\omega)$ is computed using a rotating reference frame and Taylor's frozen turbulence hypothesis. For propellers with low twist angle, $S_{F_iF_j}(\omega)$ can be approximated only by it's axial contribution $S_{F_3F_3}(\omega)$, that can be expressed as an integral over the blade radius r and the chordwise wavenumber k_2 (see [1] section 6.6.2) for waves propagating from the leading edge to the trailing edge ($k_2 \geq 0$):

$$S_{F_3F_3}(\omega) = \int_{R-b}^{R} \int_0^\infty A(r)|H(k_2)|^2 \cdot B(k_2,r)\psi_{33}(\omega,k_2,r)\, dk_2\, dr. \tag{5}$$

Here, A accounts for the axial force amplitude,

$$A(r) = \frac{1}{U_\infty}(2\pi^2\rho_\infty c(r)U(r))^2, \tag{6}$$

where $U(r)$ is the total effective speed perceived by the blades:

$$U(r) = \sqrt{U_\infty^2 + (r\Omega)^2}. \tag{7}$$

B captures inter-blade correlations,

$$B(k_2,r) = \frac{\sin^2(\pi k_2 r)}{\sin^2(\pi k_2 r/N)}. \tag{8}$$

H is the blade response function, given in the low frequency regime by the Sears function [3] of modulus approximated by [4] equations 6.4.3 and 6.4.4:

$$|H(k_2)|^2 \simeq \frac{1}{1+\pi c(r)k_2}, \quad k_2 \geq 0. \tag{9}$$

Finally, ψ_{33} is the turbulence spectrum in the rotating frame in the axial direction and will be given in the next section. This framework provides the foundation for the parametric analysis detailed later.

3. TURBULENCE MODELING

The incident turbulence is modeled as homogeneous and isotropic using the von Kármán spectrum [5] section 9.1:

$$\phi_{ij}(\boldsymbol{k}) = \frac{E(\boldsymbol{k})}{4\pi|\boldsymbol{k}|^2}\left(\delta_{ij} - \frac{k_i k_j}{|\boldsymbol{k}|^2}\right), \tag{10}$$

$$E(\boldsymbol{k}) = A_\phi \frac{|\boldsymbol{k}|^4/k_e^4}{(1+|\boldsymbol{k}|^2/k_e^2)^{17/6}}, \tag{11}$$

where $\boldsymbol{k} = (k_1, k_2, k_3)$ and the constants are defined by:

$$A_\phi = \frac{55}{9\sqrt{\pi}}\frac{\Gamma(5/6)}{\Gamma(1/3)}\frac{\overline{u^2}}{k_e}, \tag{12}$$

$$k_e = \frac{\Gamma(5/6)}{\Gamma(1/3)}\frac{\sqrt{\pi}}{L}, \quad \overline{u^2} = I_t U_\infty.$$

where I_t is the turbulent intensity. In the rotating frame, the turbulence spectrum is given by

$$\psi_{33}(\omega, k_2, r) = \phi_{33}\left(0, k_2, \frac{\omega - k_2 r\Omega}{U_\infty}\right), \tag{13}$$

providing the turbulence inputs for the the equations (5) and (4) of the noise model.

4. MODEL VALIDATION

The model is validated against Blake's analytical results [1] associated with Wojno experimental data [6] reproducing a similar configuration of the famous Sevik's study [7] with a ten-blades rotor. The parameters used for this configuration are listed in Tab. 1. The comparison, shown in Fig. 3, demonstrates good agreement, despite differences arise because Blake uses the frozen turbulence hypothesis on the chordwise wavenumber $k_2 = \omega/U(r)$ while we use the frozen turbulence hypothesis on the upstream axial wavenumber $k_3 = \omega/U_\infty$. Moreover, an offset of $10\log_{10}(U_\infty)$ has been removed from Blake's data due to the absence of normalization by U_∞ in Blake's model. This normalization is necessary when making the frozen turbulence hypothesis.

The compact source approximation leads to good predictions when the observer is located near the rotor rotational axis, where the sound level is maximum. It is underpredicted when the observer is positioned far from the axis of rotation. This underestimation is illustrated in Fig. 4, where the compact model is compared to the non-compact

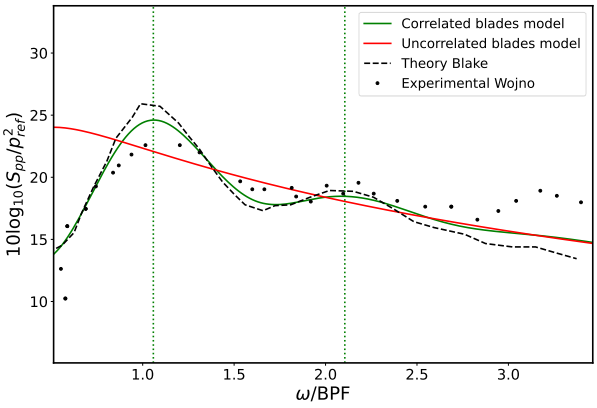

Figure 3. Comparison of radiated pressure spectrum with Blake's model and Wojno's measurements. The green solid line corresponds to the model (4) used with data from Tab. 1 and the red solid line corresponds to the same but with $B = 1$ in (5) (uncorrelated blades noise).

Table 1. Parameter values from Blake's study [1].

Parameter	Value	Unit
p_{ref}	20	μPa
ρ_∞	1.2	kg/m^3
c_∞	340	m/s
M_∞	0.037	-
I_t	0.06	-
L	1.9	cm
J_Ω	1.14	-
c	2.54	cm
R	10	cm
b	7.6	cm
N	10	-
(x_1, x_2, x_3)	(64, 0, 64)	cm

model of Raposo and Azarpeyvand [8] for an observer located at 90 degrees from the axis of rotation. Used parameters values correspond to the wind turbine case from Table 1 in [8].

Despite this, it is observed in Fig. 3 and Fig. 4, that the

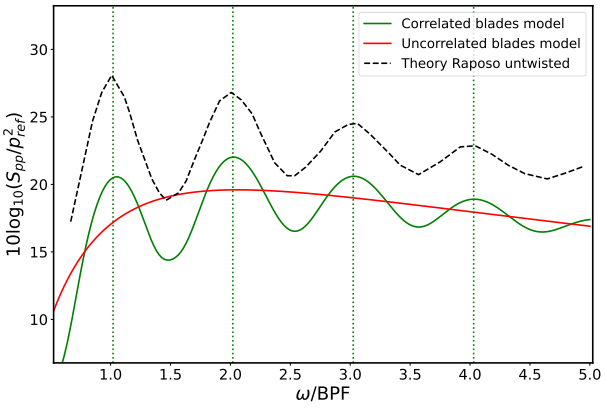

Figure 4. Comparison of radiated pressure spectrum with Raposo and Azarpeyvand's untwisted model. The green solid line corresponds to the model (4) used with data from Table 1 in [8] data and the red solid line corresponds to the same but with $B = 1$ in (5) (uncorrelated blades noise).

shape of the turbulence ingestion humps is correctly reproduced. Moreover, it is precisely this criterion (humps shape) that will be important later in the analytical definition of the emergence of these humps.

5. PARAMETRIC ANALYSIS

This section leverages the noise radiation model, specifically equation (5), to conduct a detailed parametric study of the spectral humps generated by turbulence ingestion. The analysis focuses on hump positions, their bandwidths, and the critical conditions under which these humps emerge or disappear, providing insights into noise characteristics and design implications.

5.1 Positions of the spectral humps

The positions of the spectral humps are determined by analyzing the peaks in the radiated pressure spectrum. The peak frequencies of the force spectrum (5) are derived by finding the maximum of the turbulence spectrum $\psi_{33}(\omega, k_2, r)$ with respect to ω. Setting the partial derivative $\partial\psi_{33}/\partial\omega = 0$, the resulting frequencies are:

$$\omega_{T,n} = r\Omega k_2 = nN\Omega. \tag{14}$$

These frequencies correspond to the blade-passing frequency ($BPF = N\Omega$) harmonics of harmonic number n reflecting the periodic chopping of turbulent eddies by the blades. In (14), the condition $k_2 = nN/r$ has been used indicating that the inter-blade interference term B reaches its maximum, as illustrated in the force spectrum construction process (Fig. 5).

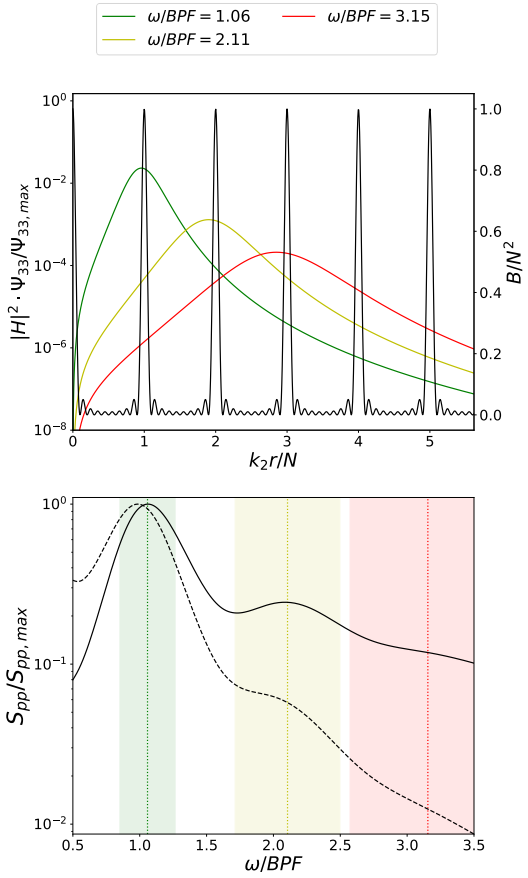

Figure 5. Normalized construction of the pressure spectrum S_{pp} (solid line lower figure) and force spectrum $S_{F_3F_3}$ (dotted line) from the integration over the chordwise wavenumber of the diffracted turbulence $|H|^2\psi_{33}$ (wide curves upper figure) times the inter-blade interference function B (narrow curve).

5.2 Bandwidths of the spectral humps

The bandwidths of the spectral humps, defined as the frequency range at half-height of their peaks, quantify their

spread and influence their distinguishability in the spectrum. For turbulence humps, the bandwidth at half-height is calculated by solving $\psi_{33}(k_2,\omega) = \frac{1}{2}\psi_{33}(k_2,\omega_T)$, yielding:

$$\Delta\omega_{T,n} \simeq U_\infty \sqrt{\frac{n^2N^2}{R^2} + k_e^2}. \tag{15}$$

This expression shows that the bandwidth increases with the inflow velocity U_∞, the harmonic number n, and the number of blades N, while being moderated by the radial position r and the turbulence integral scale $L \propto 1/k_e$. In Fig. 5, shaded zones correspond to the bandwidth predicted by (15). The relative bandwidth, normalized by the peak frequency, is:

$$\frac{\Delta\omega_{T,n}}{\omega_{T,n}} = \sqrt{\frac{J_\Omega^2}{\pi^2} + \frac{9}{16n^2N_h^2}}, \tag{16}$$

where $J_\Omega = \pi U_\infty / R\Omega$ is the propeller tip advance ratio and $N_h = N\Omega L/U_\infty$ is the chopping number introduced by Ffowcs-Williams and Hawkings in their humps prediction criterion [9] eq. 8, predicting $\Delta\omega_{T,n}/\omega_{T,n} \propto 1/N_h$ implying narrow humps when $N_h \gg 1$. This criterion is used in several studies such as Homicz and George [10], Martinez [11], Glegg et al. [12], Glegg and Devenport [4], Raposo and Azarpeyvand [8]. Unlike Ffowcs-Williams and Hawkings prediction, the present criterion (16) indicates a stronger dependence on the advance ratio J_Ω, meaning that a large N_h does not necessarily imply narrow humps. Note that this new formulation is equivalent to that of Ffowcs-Williams and Hawkings when $J_\Omega \to 0$.

5.3 Hump emergence criteria

The emergence of spectral humps is a pivotal concept in this study, as it directly informs strategies for noise control in propeller design. Turbulence humps are distinguishable in the spectrum when their bandwidths do not exceed the frequency spacing between consecutive humps, given by $N\Omega$. If the bandwidth $\Delta\omega_{T,n}$ surpasses this threshold, the humps overlap and the spectrum flattens into a broadband signature. Mathematically, this condition is expressed as:

$$\frac{\Delta\omega_{T,n}}{N\Omega} > 1. \tag{17}$$

Substituting the bandwidth from Equation (15), this inequality becomes:

$$J_\Omega > \frac{\pi}{\sqrt{n^2 + \frac{r^2k_e^2}{N^2}}}, \tag{18}$$

meaning that the n-th turbulence hump vanishes if J_Ω is superior to a critical advance ratio, as their bandwidth exceeds the BPF spacing. This critical advance ratio is defined by:

$$J_{\Omega,c}(n) = \frac{\pi}{\sqrt{n^2 + \frac{r^2k_e^2}{N^2}}}. \tag{19}$$

The most restrictive case occurs at the first harmonic ($n = 1$), where overlap eliminates all subsequent humps if exceeded. Fig. 6 illustrates this effect, showing how increasing J_Ω beyond the critical value leads to a loss of distinct humps. A trend consistent with experimental observations where humps disappear at higher inflow velocities relative to rotation speed even with the number N_h being fixed (see [8] section 4.2). Given the expression (19), we can reformulate the relative bandwidth (15) only in terms of the advance ratio :

$$\frac{\Delta\omega_{T,n}}{\omega_{T,n}} = \frac{J_\Omega}{nJ_{\Omega,c}(n)}. \tag{20}$$

Physically, a high J_Ω implies a faster axial inflow U_∞ compared to the rotational speed $R\Omega$, increasing the frequency at which eddies are chopped and thus broadening the spectral humps to the shape of the turbulence spectrum. For the Blake's parameters in Tab. 1, $J_{\Omega,c}(1) \simeq 2.92$, $J_{\Omega,c}(2) \simeq 1.54$ and $J_{\Omega,c}(3) \simeq 1.04$. Thus the experimental $J_\Omega = 1.14$ suggests overlap after the second humps, which is what we observe in Fig. 3. This criteria for hump emergence offer actionable insights for propeller design. Optimizing parameters like blade count N, turbulence integral scale L, and rotor's radius R can suppress humps, by diminishing the critical advance ratio $J_{\Omega,c}$ an thus reducing ship's detectability.

5.4 Spectral humps perceived by the observer

The spectrum perceived by the observer is that radiated by the pressure fluctuations (4) resulting from the propagation and deformation of the force spectrum from the blades such that $S_{pp} \propto \omega^2 S_{F_3F_3}$. The frequency of the perceived humps $\omega_{p,n}$ (peaks of S_{pp}) is therefore different from that of the turbulent humps (peaks of $S_{F_3F_3}$). The link between the perceived humps and turbulence's humps is established by expressing the peaks of S_{pp} in function of the peaks of $S_{F_3F_3}$ using (4) and (2):

$$\omega_{p,n} \simeq \frac{\omega_{T,n}}{2} + \frac{1}{2}\sqrt{\omega_{T,n}^2 + \frac{\Delta\omega_{T,n}^2}{\ln(2)}}. \tag{21}$$

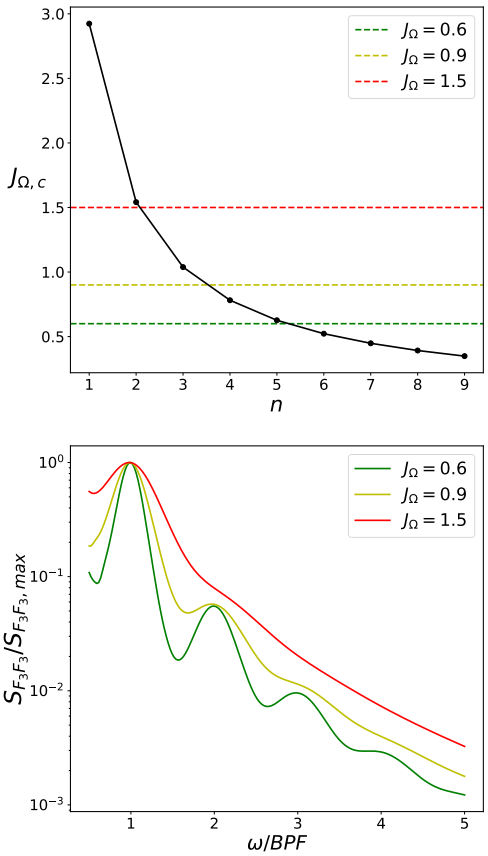

Figure 6. Impact of critical advance ratio on turbulence hump visibility, showing $J_{\Omega,c}$ versus harmonic number (upper figure) and normalized force spectrum flattening (lower figure). Parameters values are from Tab. 1.

It is therefore noted that the position of the humps perceived by the observer is slightly shifted to the right (higher frequencies) as the humps bandwidths increases, consequence of the propagation from the propeller to the observer. This phenomenon is illustrated in Fig. 5. Recently, this 'blue shifting' phenomenon has been qualitatively described by Huang [13] and numerically studied by Qin et al. [14]. Moreover, Martinez [15] made a theory for large N, predicting the first hump's 'blue shifting' of the force spectrum $S_{F_3F_3}$ (i.e. on the shift of $\omega_{T,n} > nN\Omega$ which is not seen here) but not for the pressure spectrum S_{pp} (i.e. not for $\omega_{p,n}$). By injecting the expression (15) obtained for the bandwidths into (21), we derive the explicit expression of $\omega_{p,n}$ as a function of the problem's parameters:

$$\omega_{p,n} = \frac{\omega_{T,n}}{2}\left(1 + \sqrt{1 + \frac{1}{n^2 \ln(2)}\frac{J_\Omega^2}{J_{\Omega,c}^2}}\right). \qquad (22)$$

with $\omega_{T,n} = nN\Omega$. It is interesting to note that there exists a maximum shift, dependent only on n, when $J_\Omega = J_{\Omega,c}$, since the n-th peak overlaps for higher advance ratio (when $J_\Omega > J_{\Omega,c}$). The first peak satisfies $\max(\omega_{p,1}) \simeq 1.28\omega_{T,1}$, corresponding to a maximum shift of 28%. The maximum shift then rapidly decreases with n, such that $\max(\omega_{p,2}) \simeq 1.08\omega_{T,2}$ and $\max(\omega_{p,3}) \simeq 1.04\omega_{T,3}$, corresponding to 8% and 4%, respectively. For the parameters of Tab. 1, we obtain a shift of $\omega_{p,1} \simeq 1.06\omega_{T,1} = 1.06BPF$, which is a better prediction of the experimental shift observed in Fig. 3 (dotted vertical lines).

6. SPECIFIC CASES

In this last section, an analysis of special cases of the previous model is presented to demonstrate its equivalence with theories in the literature dealing with limit cases.

6.1 Static propeller

When the propeller is static ($\Omega = 0$) and has only one blade ($N = 1$), the model reduces to leading edge diffraction noise as in section 14.3 of [4]:

$$S_{F_2F_2}(\omega) = 4\pi^4 \rho_\infty^2 c^2 U_\infty b \left|H\left(\frac{\omega}{U_\infty}\right)\right|^2 \Phi_{22}\left(0, \frac{\omega}{U_\infty}\right),$$

$$S_{pp}(\boldsymbol{x}, \omega) = \left(\frac{\omega x_2}{8\pi^2 c_\infty |\boldsymbol{x}|^2}\right)^2 S_{F_2F_2}(\omega). \qquad (23)$$

with $\Phi_{22}(k_1, k_3) = \int_{-\infty}^{+\infty} \phi_{22}(k_1, k_2, k_3) dk_2$ the two-dimensional turbulence spectrum in the blade plane. This model thus reproduces the result of Glegg and Devenport [4], for a fixed wing in turbulent flow, modulo a factor 2π, given that the normalization of the Fourier transform used is not the same as here (see appendix).

6.2 Uncorrelated blades

The cross-correlation function between the blades B is responsible for the periodic reproduction of the turbulence spectrum (and thus the production of the humps) in (5).

Setting $B = 1$ amounts to neglecting the interaction between the incident turbulent field and the periodicity of the blade passage, which thus eliminates the humps while still preserving the average trend of the spectrum (red mean line without humps in Fig. 3 and 4) given by the diffraction of the turbulence corresponding to $|H|^2 \cdot \psi_{33}$ in (5). This uncorrelated approach has already been theorized by Sevik during his experiment in 1971 [7].

7. CONCLUSION

This study has successfully developed a simplified analytical model to predict turbulence ingestion noise for marine propellers, focusing on the characterization of spectral humps. The key steps undertaken include: (1) the adaptation of the Ffowcs-Williams and Hawkings formulation to model acoustic radiation from moving surfaces, incorporating a homogeneous and isotropic von Kármán turbulence spectrum; (2) validation of the model against Blake's and Raposo's analytical and experimental results, confirming its ability to reproduce hump shapes despite some underpredictions in non-compact scenarios; (3) a detailed parametric analysis to determine hump positions, bandwidths, and emergence criteria, introducing a refined critical advance ratio $J_{\Omega,c}(n)$ that improves upon the original Ffowcs-Williams and Hawkings criterion; and (4) an exploration of special cases, such as static propellers and uncorrelated blades, demonstrating equivalence with established theories. Future works will focus on implementing realistic propeller geometry (with twist, sweep and skew angles, etc.) into the models and relaxing compacity hypothesis to study the potential influence on humps positions, and bandwidths.

8. APPENDIX

8.1 Fourier transform conventions

For the Fourier transforms in time and space, the following conventions and notations are used:

$$\widehat{f}(\omega) = \frac{1}{2\pi} \int_{-\infty}^{+\infty} f(t) e^{i\omega t} dt,$$

$$f(t) = \int_{-\infty}^{+\infty} \widehat{f}(\omega) e^{-i\omega t} d\omega$$

9. REFERENCES

[1] W. K. Blake, "Chapter 6 - noise from rotating machinery," in *Mechanics of Flow-Induced Sound and Vibration, Volume 2 (Second Edition)* (W. K. Blake, ed.), pp. 505–658, Academic Press, second edition ed., 2017.

[2] M. Goldstein, "Unified approach to aerodynamic sound generation in the presence of solid boundaries," *The Journal of the Acoustical Society of America*, vol. 56, pp. 497–509, 08 1974.

[3] W. R. Sears, "Some aspects of non-stationary airfoil theory and its practical application," *Journal of the Aeronautical Sciences*, vol. 8, no. 3, pp. 104–108, 1941.

[4] S. Glegg and W. Devenport, "Aeroacoustics of low mach number flows," Academic Press, 2017.

[5] S. A. Glegg, W. Devenport, and N. Alexander, "Broadband rotor noise predictions using a time domain approach," *Journal of Sound and Vibration*, vol. 335, pp. 115–124, 2015.

[6] J. P. Wojno, T. J. Mueller, and W. K. Blake, "Turbulence ingestion noise, part 2: Rotor aeroacoustic response to grid-generated turbulence," *AIAA Journal*, vol. 40, no. 1, pp. 26–32, 2002.

[7] M. Sevik, "Sound radiation from a subsonic rotor subjected to turbulence," Fluid Mechanics, Acoustics and Design of Turbomachinery NASA SP-304, 1974.

[8] H. Raposo and M. Azarpeyvand, "Turbulence ingestion noise generation in rotating blades," *Journal of Fluid Mechanics*, vol. 980, 02 2024.

[9] W. J. E. Ffowcs and D. L. Hawkings, "Theory relating to the noise of rotating machinery," *J. Sound Vib*, pp. 10–21, 1969.

[10] G. Homicz and A. George, "Broadband and discrete frequency radiation from subsonic rotors," *Journal of Sound and Vibration*, vol. 36, no. 2, pp. 151–177, 1974.

[11] R. Martinez, "Asymptotic theory of broadband rotor thrust, part i: Manipulations of flow probabilities for a high number of blades," *Journal of Applied Mechanics*, vol. 63, pp. 136–142, 03 1996.

[12] S. Glegg, M. Morton, and W. Devenport, "Rotor inflow noise caused by a boundary layer: Theory and examples," in *18th AIAA/CEAS Aeroacoustics Conference*, (Colorado Springs, CO), American Institute of Aeronautics and Astronautics, June 2012.

[13] X. Huang, "Convolution for haystacking in turbulence-ingesting rotor noise," *AIAA Journal*, vol. 61, 11 2023.

[14] D. Qin, O. Stalnov, and X. Huang, "Numerical investigation of parameters influencing the turbulence-ingesting noise of a ten-bladed propeller," *Ocean Engineering*, vol. 300, p. 117237, 2024.

[15] R. Martinez, "Asymptotic theory of broadband rotor thrust, part ii: Analysis of the right frequency shift of the maximum response," *Journal of Applied Mechanics*, vol. 63, pp. 143–148, 03 1996.